Redox Control of Particle Deposition from Drying Drops

Pauline E. Galy, Tiffany Guitton-Spassky, Catherine Sella, Laurent Thouin, Maxime R. Vitale, and Damien Baigl*

Cite This: *ACS Appl. Mater. Interfaces* 2022, 14, 3374−3384

Read Online

| ACCESS | Metrics & More | Article Recommendations | Supporting Information |

ABSTRACT: The coffee-ring effect (CRE), which denotes the accumulation of nonvolatile compounds at the periphery of a pinned sessile drying drop, is a universal and ubiquitous yet complex phenomenon. It is crucial to better understand and control it, either to avoid its various deleterious consequences in many processes requiring homogeneous deposition or to exploit it for applications ranging from controlled particle patterning to low cost diagnostics. Here, we report for the first time the use of a reduction−oxidation (redox) stimulus to cancel the CRE or harness it, leading to a robust and tunable control of particle deposition in drying sessile drops. This is achieved by implementing redox-sensitive ferrocenyl cationic surfactants of different chain lengths in drying drops containing anionic colloids. Varying surfactant hydrophobicity, concentration, and redox state allows us not only to control the overall distribution of deposited particles, including the possibility to fully cancel the CRE, but also to modify the microscopic organization of particles inside the deposit. Notably, with all other parameters being fixed, this method allows the adjustment of the deposited particle patterns, from polycrystalline rings to uniform disks, as a function of the oxidation rate. We show that the redox control can be achieved either chemically by the addition of oxidants or electrochemically by applying a potential for additive-free and reversible actuation in a closed system. This correlation between the redox state and the particle pattern opens a perspective for both redox-programmable particle patterning and original diagnostic applications based on the visual determination of a redox state. It also contributes to clarify the role of surfactant charge and its amphiphilic character in directing particle deposition from drying suspensions.

KEYWORDS: coffee-ring effect, colloids, ferrocene, redox-sensitive, surfactants, evaporation, particle patterning
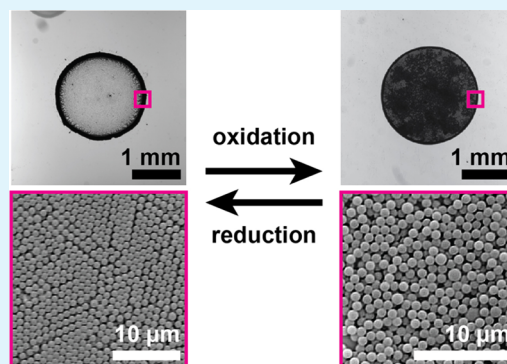
INTRODUCTION

When a drop of a suspension of nonvolatile compounds is deposited on a solid surface, its evaporation leads to a ring-shaped deposit. This ubiquitous phenomenon, which occurs when the contact line is pinned on the substrate, is called the coffee-ring effect (CRE).[1] It occurs not only with practically any type of liquid containing nonvolatile solutes like colloids, nanoparticles, or proteins but also with insoluble particle-laden liquids dissolving in another partially miscible liquid phase (liquid−liquid CRE).[2] This has led to a rich literature devoted to this phenomenon, which remains, however, neither fully understood nor predictable because of its multiscale, multi-component, and unsteady characters.[3,4] As many technical processes are relying on deposition of homogeneous layers of a material during solution evaporation, the CRE appears as a serious obstacle for a plethora of applications with deleterious impacts in industrial fields ranging from inkjet printing[5] to biotechnologies.[6−8] Conversely, it can be seen as a tool[9] to organize particles on surfaces[10−13] or an innovative solution for low cost diagnostic applications.[14−18] There is thus a general quest for methods to understand, cancel, and/or control this phenomenon. Perturbing evaporation or contact line pinning using external triggers is shown to be efficient[19−21] but is not easily implementable. In contrast, formulation approaches using proper additives, such as polymers or binary mixtures,[22,23] offer easy solutions but can perturb the system at high concentrations and usually lack external addressability. Among additives, surfactants are thus particularly interesting candidates, first because they can be effective at a low concentration (typically micro- to millimolar). Indeed, surfactants have been shown to be very efficient to control or cancel the coffee-ring effect, either by creating interfacial energy gradients leading to Marangoni flows[24] or by inducing particle adsorption at the drop water/air interface through a combination of electrostatic and hydrophobic effects.[9,25,26] It is generally believed that a more hydrophobic surfactant is more efficient, i.e., a lower concentration is needed to affect or cancel the coffee-ring effect because it has stronger surface activity
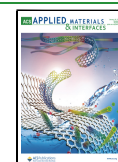
and its cooperative assembly on oppositely charged particles is favored.[26] But what would happen for a surfactant of a given chain length but higher electrostatic charge, which would result in a lower hydrophobicity but higher electrostatic interaction? This open question has yet to be solved if one wants to understand how charged surfactants determine the patterns of particle deposits from drying suspension drops. Second, some surfactants can be stimulus-responsive, thus offering the advantageous possibility to dynamically tune their properties in a user-controlled fashion. This was for instance successfully applied with photosensitive surfactants[27,28] to efficiently photocontrol the CRE[25] and to direct particle assembly on surfaces[12,13] using an external light stimulus. Such an approach offered excellent and remote spatiotemporal control of particle deposition from drying drops but required the implementation of azobenzene-containing molecules as well as samples resilient to UV irradiation. Surprisingly, no other types of stimulus-responsive surfactants have been explored as possible alternatives to photosensitive ones, and controlling the CRE has thus been mainly limited to more conventional formulation approaches. To address the 2-fold challenge of rationalizing the roles of surfactant amphiphilicity and electrostatics in the CRE and exploring a totally new way of controlling it, we studied for the first time the deposition pattern from aqueous sessile drops containing particles and a surfactant with a charge and amphiphilic character that depends on its reduction–oxidation (redox) state. Redox-sensitive surfactants have been investigated for various applications, such as stimulus-responsive micelles and emulsions,[29−33] DNA compaction,[34] or interfacial flow control,[35−37] but have never been reported for directing the deposition of particles in general or controlling the CRE in particular. In this work, we synthesized and characterized redox-sensitive cationic surfactants of different chain lengths prior to analyzing the patterns obtained from evaporating drops containing anionic particles and the synthesized surfactants at different concentrations and redox states. This allowed us to efficiently control the drop deposition patterns, including the full cancellation of the CRE, with a redox stimulus for the first time. At a fundamental level, this study also contributed to disentangle the respective roles of electrostatics and amphiphilicity in surfactant-based control of particle deposition from drying drops.

MATERIALS AND METHODS

Materials. Milli-Q water (Millipore, 18.2 MΩ·cm) was used for all experiments. A suspension of negatively charged polystyrene particles (diameter 1 μm, concentration 4 wt %) bearing a high density of carboxyl functional groups on their surface was purchased from Life Technologies (CML latex, catalogue number C37255) and used as received. Prior to each experiment, the particle suspension was mixed by vortexing (1 min), sonicated in an ultrasound bath (1 min), and vortexed again (30 s). Lithium sulfate monohydrate (CAS 10102-25-7, Merck, purity > 99%), iron(III) sulfate (CAS 15244-10-7, Merck, purity > 97%), iron(II) sulfate heptahydrate (CAS 7782-63-0, Merck, purity > 99%), trimethylamine solution (CAS 75-50-3, 4.2 M in ethanol), (6-bromohexyl)-ferrocene (CAS 136237-36-0, Merck), 11-bromoundecanoic acid (CAS 2834-05-1, Merck, purity > 99%), thionyl chloride (CAS 7719-09-7, Merck, purity > 99%), N,N-dimethylformamide (DMF, CAS 68-12-2, Merck, purity > 99%), aluminum chloride (CAS 7446-70-0, Merck, purity > 99%), ferrocene (CAS 102-54-5, Merck, purity > 98%), sodium borohydride (CAS 16940-66-2, Merck, purity > 98%), toluene (CAS 108-88-3, Carlo Erba, purity > 95%), diethyl elther (DE), dichloroethane (DCE, CAS 107-06-2, Carlo Erba, purity > 95%), dichloromethane (DCM, CAS 75-09-2, Carlo Erba, purity > 95%), ethanol (CAS 64-17-5, Merck,

purity > 98%), heptane (CAS 142-82-5, Carlo Erba, purity > 95%), petroleum ether 30−40 °C (PE, CAS 64742-49-0, Carlo Erba, purity > 95%), and *tert*-butyl methyl ether (TBME, CAS 1634-04-4, Carlo Erba, purity > 95%) were all used without purification. Tetrahydrofuran (THF, CAS 109-99-9, Carlo Erba, purity > 98%) was freshly distilled from a mixture with solid sodium before use.

F_6TAB^+ Synthesis. (6-Ferrocenylhexyl) trimethyl ammonium bromide (F_6TAB^+) was synthesized following the procedure from Saji et al.[31] (see Figure 2A). In a 25 mL round-bottom flask, 1.8 mmol (6-bromohexyl)-ferrocene (**1**) was introduced. An excess of 3.4 mL of trimethylamine in 4.2 M solution in ethanol was added. Then, 3 mL of pure ethanol was added and the mixture was stirred for 5 days at room temperature. The mixture was evaporated under a vacuum at 40 °C to remove ethanol to get yellow oil. A yellow solid was crystallized by the addition of 3 mL of hexane. The solid was washed in 3 × 500 μL of hexane and dried under vacuum. Recrystallization in a mixture 1:1 acetone/hexane gave 617 mg of pure F_6TAB^+ (**2**) as a yellow solid (yield 86%), with ^1H NMR (MeOD-D4) δ 4.0−4.1 (m, 9 H, ferrocene), 3.3 (m, 2 H, $-CH_2-N^+(CH_3)_3$), 3.1 (s, 9 H, $-N^+(CH_3)_3$), 2.4 (t, 2 H, ferrocene-CH_2-), 1.8 (q, 2 H, $-CH_2-CH_2N^+(CH_3)_3$), and 1.3−1.6 (m, 16 H, $-CH_2-CH_2-CH_2-$). IR data agreed with the product structure. The solid was permanently kept under argon. By diluting in pure water, it gave a pure reduced F_6TAB^+ solution that was very slowly oxidized in time. The solubility of F_6TAB^+ was determined to be around 30 mM.

$F_{11}TAB^+$ Synthesis. *Step 1.* (11-Ferrocenylundecyl)trimethyl ammonium bromide ($F_{11}TAB^+$) was synthesized following the original procedure from Saji et al.[31] but with improvements (see Figure 3A). For the first step, the procedure was improved from García-Barrantes et al.[38] In a 200 mL round-bottom flask under argon and linked to a gas oil bubbler, 24.6 g of 11-bromoundecanoic acid (**3**) was mixed with 20 mL of thionyl chloride (1 equiv) in 110 mL of anhydrous toluene. Some drops of DMF were added, and the mixture was stirred for 3 h at 40 °C. The reaction was followed by thin-layer chromatography (solvent toluene). The mixture was evaporated under reduced pressure, 20 mL of toluene was added under argon, and the mixture was evaporated again. The process was repeated two times. Acyl chloride (**4**) was obtained as a slightly yellow residue and identified with ^1H NMR (CDCl$_3$) δ 1.3−2.3 (m, 16 H, Br-CH$_2$-(CH$_2$)$_8$-CH$_2$-COCl), δ 2.9 (t, 2 H, $-CH_2$-COCl), and δ 3.4 (t, 2 H, $-CH_2$-Br). The yield was 86%.

Step 2. Typically, 20.4 g of acyl chloride (**4**) was dissolved in 100 mL of anhydrous dichloromethane and 10.1 g of aluminum chloride (1 equiv) was added. In another round-bottom flask under argon, 14.7 g of ferrocene (1 equiv) was dissolved in 150 mL of anhydrous dichloromethane. The acyl chloride mixture was then added dropwise to the ferrocene mixture for around 30 min at 0 °C. The resulting solution was stirred for 1 h at 0 °C and followed by thin-layer chromatography (solvent toluene). When all the acyl chloride was consumed, around 100 mL of HCl at 2 M was gently added until the solution ceased to degas. Organic and aqueous phases were separated. The aqueous phase was extracted with three fractions of 20 mL of *tert*-butyl methyl ether. Organic phases were dried with magnesium sulfate and evaporated under reduced pressure. Product (**5**) was purified by column chromatography (silica, PE, then TBME and DE) and was identified with ^1H NMR (CDCl$_3$) δ 1.2−1.5 (m, 10 H, Br-CH$_2$-CH$_2$-(CH$_2$)$_5-$), δ 1.7 (m, 2 H, Br-CH$_2$-CH$_2$-(CH$_2$)$_5$-CH$_2-$), δ 1.8−1.9 (m, 2 H, Br-CH$_2$-CH$_2$-(CH$_2$)$_5-$), δ 2.7 (t, 2 H, Fc-CO-CH$_2-$), δ 3.4 (t, 2 H, Br-CH$_2-$), and δ 4.2−4.8 (3×s, 9 H, **Fc−**). The yield was 83%.

Step 3. This step was slightly improved from the Li et al. procedure.[39] In a 1 L round-bottom flask under argon and equipped with a gas oil bubbler, 26.2 g of ferrocene carbonyl product (**5**) was dissolved in 66 mL of dry tetrahydrofuran. In a 500 mL round-bottom flask under argon, 9.4 g of sodium borohydride (4 equiv) and 16.3 g of aluminum chloride (2 equiv) were dissolved in 70 mL of dried tetrahydrofuran. Then, the ferrocene carbonyl mixture was added dropwise for around 1 h at 0 °C with strong magnetic stirring under argon. The reaction was followed by thin-layer chromatography (solvent PE/DE 20:1). Then, 105 mL of water was added dropwise to
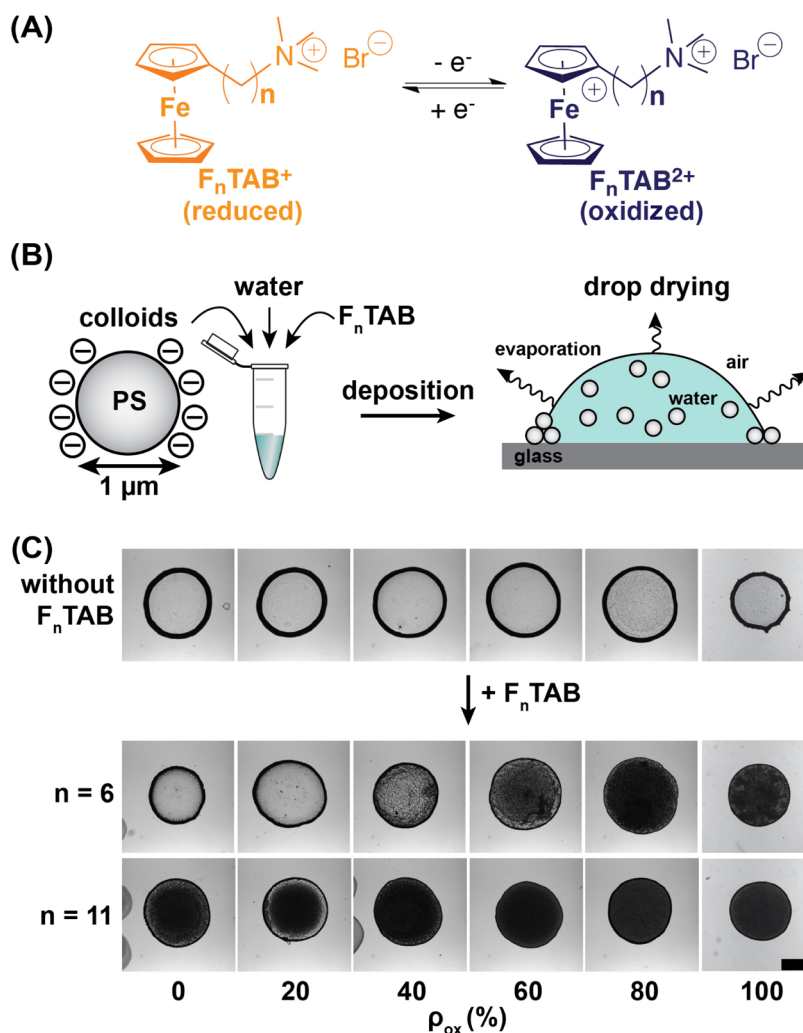
Figure 1. Redox control of the coffee-ring effect. (A) Reduced and oxidized forms of (*n*-ferrocenyl-*n*-alkyl)trimethyl ammonium bromide (F$_n$TAB) redox-sensitive surfactant. (B) Scheme of the setup for particle deposition: evaporation in air of a 1 μL sessile drop on glass containing anionic polystyrene particles (1 μm diameter, 4 mg·mL^{-1}) and F$_n$TAB. (C) Representative transmission microscopy images of the deposits obtained in the absence of F$_n$TAB (top), with the addition of 80 μM of F$_6$TAB (middle) or F$_{11}$TAB (bottom) at oxidation rates (ρ_{ox} = [F$_n$TAB^{2+}]/[F$_n$TAB]) varying from 0% (pure F$_n$TAB$^+$) to 100% (pure F$_n$TAB^{2+}). Actual values of ρ_{ox} are given in Table S1. The scale bar is 1 mm.

the mixture at 0 °C with strong stirring. Warning: the reaction is highly exothermic. Once the mixture became less reactive, 150 mL of HCl at 1 M was added. Phases were separated and the aqueous phase was extracted with three 20 mL fractions of PE. Organic phases were dried with magnesium sulfate and evaporated under reduced pressure. Crude orange-yellow oil was obtained. Product (**6**) was recrystallized in PE and filtrated through silica frittered glass and finally identified with ^{1}H NMR (CDCl$_3$) δ 1.2−1.6 (m, 12 H, Br-CH$_2$-CH$_2$-(**CH$_2$**)$_6$−), δ 1.8−1.9 (q, 2 H, Br-CH$_2$-**CH$_2$**-(CH$_2$)$_5$−), δ 2.3 (t, 2 H, Fc-**CH$_2$**−), δ 3.4 (t, 2 H, Br-**CH$_2$**−), and δ 4.1 (s, 9 H, **Fc**). The yield was 70%.

Step 4. Typically, 17.7 g of alkyl bromide (**6**) was mixed with 100 mL of trimethylamine solution in ethanol (8 equiv) and 100 mL of THF. The mixture was stirred under reflux at 40 °C for one day. Then, it was evaporated under a vacuum. Product (**7**) was recrystallized after mixing vigorously in TBME. It was filtrated, dried overnight on a Schlenk line, and identified with ^{1}H NMR (MeOD-4D) δ 1.3−1.6 (m, 8 H, Br(CH$_3$)$_3$N-CH$_2$-CH$_2$-(**CH$_2$**)$_8$−), δ 1.8 (q, 2 H, Br(CH$_3$)$_3$N-CH$_2$-**CH$_2$**−), δ 2.32 (t, 2 H, Fc-**CH$_2$**−), δ 3.1 (s, 9 H, Br(**CH$_3$**)$_3$N−), δ 3.33 (t, 2 H, Br(CH$_3$)$_3$N-**CH$_2$**−), and δ 4.1 (s, 9 H, **Fc**−). The yield was 99% and the synthesis overall yield was 49%.

Electrochemical Properties. The electrochemical cell was a 50 mL triple neck flat-bottom flask filled with a day-made 30 mL solution of 5 mM F$_6$TAB with 100 mM Li$_2$SO$_4$ as an electrolyte. The

electrodes were a platinum disk (50 μm diameter) as the working electrode, a platinum wire (1 mm diameter) as the counter electrode, and a silver reference electrode (RE) covered with silver oxide. All electrochemical experiments were performed at room temperature using a potentiostat PGSTAT 30 controlled by GPES 4.9 software. Cyclic voltammetry was carried out between −0.25 and +0.4 V at 10 mV·s^{-1} scan rate without stirring (Figure 2B). The same procedure was used for 2 mM F$_{11}$TAB (Figure 3B).

Electrochemical Oxidation. Experiments were performed at a constant potential using the same electrochemical cell with a strong magnetic stirring. A platinum grid with a high surface area of ∼3 cm^2 was used as the working electrode. The counter electrode was inserted in a separate compartment filled with 100 mM Li$_2$SO$_4$ electrolyte. The F$_6$TAB solutions were oxidized to F$_6$TAB^{2+} at E = +0.25 V or reduced to F$_6$TAB$^+$ at E = −0.25 V for 3600 s.

UV−Visible Absorbance and Absorption Coefficients. Absorbance spectra were obtained with a BioSpectrometer (Eppendorf). For F$_n$TAB solutions at various oxidation rates in pure water, water was used as a reference. For F$_n$TAB solution containing the electrolyte Li$_2$SO$_4$ at 100 mM, a solution of 100 mM Li$_2$SO$_4$ was used as a reference. Measurements were performed in a 1 cm wide plastic cuvette. Molar extinction coefficients of F$_6$TAB$^+$ (reduced), F$_6$TAB^{2+} (oxidized), F$_{11}$TAB$^+$ (reduced), and F$_{11}$TAB^{2+} (oxidized) at 437 and 627 nm were deduced from absorbance spectra
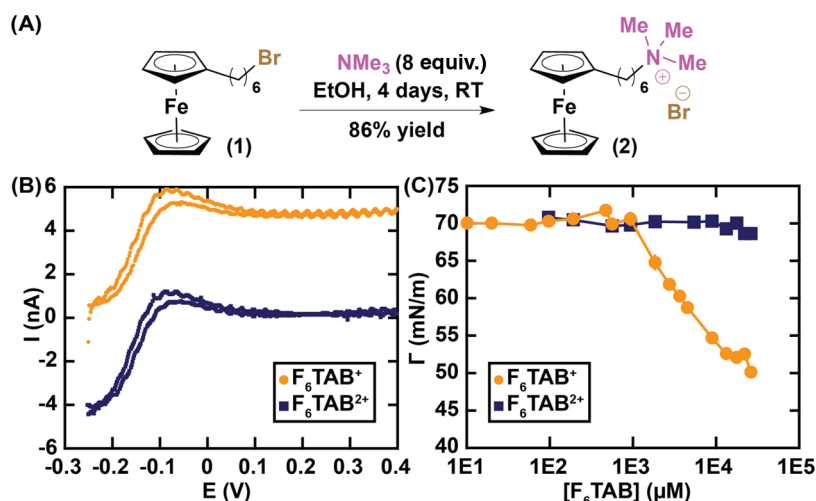
Figure 2. Synthesis and properties of F₆TAB. (A) Synthesis scheme. (B) Steady-state voltammograms (current vs potential) of the reduced (F₆TAB⁺, orange disks) and oxidized (F₆TAB²⁺, blue squares) forms of F₆TAB (5 mM) in an aqueous solution of Li₂SO₄ (100 mM). (C) Interfacial energy in air (Γ) of water containing F₆TAB⁺ or F₆TAB²⁺, as a function of the surfactant concentration.

of solutions of F_nTAB (5 mM for $n = 6$; 2 mM for $n = 11$) in 100 mM Li₂SO₄ and at a defined oxidation rate controlled by chronoamperometry (Figure S2).

Chemical Oxidation. Six mother solutions of 2 mM F_nTAB were prepared in pure water. Each of them had a different oxidation rate {0, 0.20, 0.40, 0.60, 0.80, 1} obtained by the addition of equivalent quantity of an iron(III) ion from Fe₂(SO₄)₃. Iron(III) reacted fast and totally with F_nTAB⁺ to give iron(II) and F_nTAB²⁺ (Figure S3). A series of control solutions were made without F_nTAB and with water and iron(III) at the corresponding concentrations.

Sample Preparation and Drop Deposition. Mother F_nTAB solutions (2 mM), oxidized if necessary as described above, were diluted in water and mixed with particle suspension to get the desired F_nTAB concentration and a final particle concentration of 4 mg·mL⁻¹. All drops have been deposited in a volume of 1 μL (Eppendorf micropipette) on rectangular glass coverslips (24 × 60 mm, Menzel-Gläser) for all experiments except for scanning electron microscopy (SEM), where circular glass coverslips (Menzel-Gläser, 1.5 cm in diameter) were used. Drop evaporation was achieved at 21 ± 2 °C and 45 ± 10% relative humidity under a box to avoid airflow and dust contamination during drying.

Drops and Deposits Observation. All of the samples have been observed using an inverted epifluorescence microscope (Observer D1, Zeiss), equipped with an sCMOS camera (Zyla 4.2 Plus, Andor Technology). For the acquisition of whole deposits, a 4× magnification objective was used (UPlanFLN 4×, Olympus). For scanning electron microscopy (SEM) imaging, a gold layer was first deposited on the samples (sputtering system, 125 mA, 60 s) and then imaged at an incident angle of 90° with a tabletop SEM microscope (Hitachi, TM3030) at magnification ranging from 30× to 1000×.

Tensiometry. Interfacial energy has been recorded using a drop shape analyzer (DSA 30, Krüss). A 4 μL drop of desired concentration of F_nTAB and/or iron(III) from Fe₂(SO₄)₃ was generated at room temperature (21 ± 4 °C and 45 ± 20% relative humidity). The drop shape was analyzed using the instrument software (DSA4, Krüss) to extract the water/air interfacial energy (Γ). The drop was protected from airflows and we waited about 10 min to reach stabilization and measure the equilibrium value of Γ.

ζ-Potential. ζ-Potential measurements have been conducted on a Zetasizer Nano ZS (Malvern Instruments). F_nTAB was diluted at a desired concentration with iron(III) from Fe₂(SO₄)₃ and mixed with latex colloids. Because the concentration used in CRE experiments was too high to get reliable measurements, we used a final concentration of 0.4 mg·mL⁻¹, which was 10 times less than that in CRE experiments. The final solution was agitated 30 s before the measurement. The volume of the sample was 850 μL. Experiments

were conducted at room temperature (25 ± 1 °C). Each ζ-potential measurement was a mean from 10 to 50 individual measurements. This was repeated three times for each condition and averaged to give the ζ-potential values plotted in Figure S5.

■ RESULTS AND DISCUSSION

Figure 1 depicts our experimental system and shows the main result. We used two redox-sensitive surfactants, (6-ferrocenylhexyl)trimethyl ammonium bromide and (11-ferrocenylundecyl)trimethylammonium bromide surfactants referred to as F_nTAB with n equals 6 and 11, respectively. The reduced form, referred to as F_nTAB⁺, has a neutral ferrocenyl group at the extremity of its hydrophobic tail and a quaternary ammonium bromide polar head (Figure 1A, left). The oxidation of the ferrocenyl group leads to the oxidized form of F_nTAB, referred to as F_nTAB²⁺, which contains an additional positive charge on its tail (Figure 1A, right). To evaluate how a redox state can affect the CRE, a colloidal suspension containing anionic particles at a fixed concentration was supplemented with F_nTAB at different oxidation rates and concentrations (Figure 1B, left). A drop (1 μL) of this mixture was deposited on a glass substrate and allowed to evaporate under room conditions (21 ± 2 °C and 45 ± 10% relative humidity) and protected from airflows (Figure 1B, right). Under these conditions, full evaporation of the drop was achieved in about 30−40 min. In the absence of F_nTAB, all resulting particle deposits displayed a characteristic ring shape due to the evaporation-driven transport of particles toward the pinned contact line (Figure 1C, top), in agreement with a conventional and strong CRE.[1,4] In contrast, the addition of F_nTAB led to a dramatic effect on the morphology of the dry deposit. For instance, with 80 μM of F₆TAB, the deposition pattern evolved from a ring to a disk shape when the fraction of the oxidized form of the surfactant increased from 0% (fully reduced form, F₆TAB⁺ only) to 100% (fully oxidized form, F₆TAB²⁺ only) (Figure 1C, middle). This was also dependent on the amphiphilic character of the surfactant as, for the same surfactant concentration, only disks were obtained with the more hydrophobic F₁₁TAB (Figure 1C, bottom). To our knowledge, this is the first time that the CRE is controlled through a redox stimulation and the detailed analysis of this
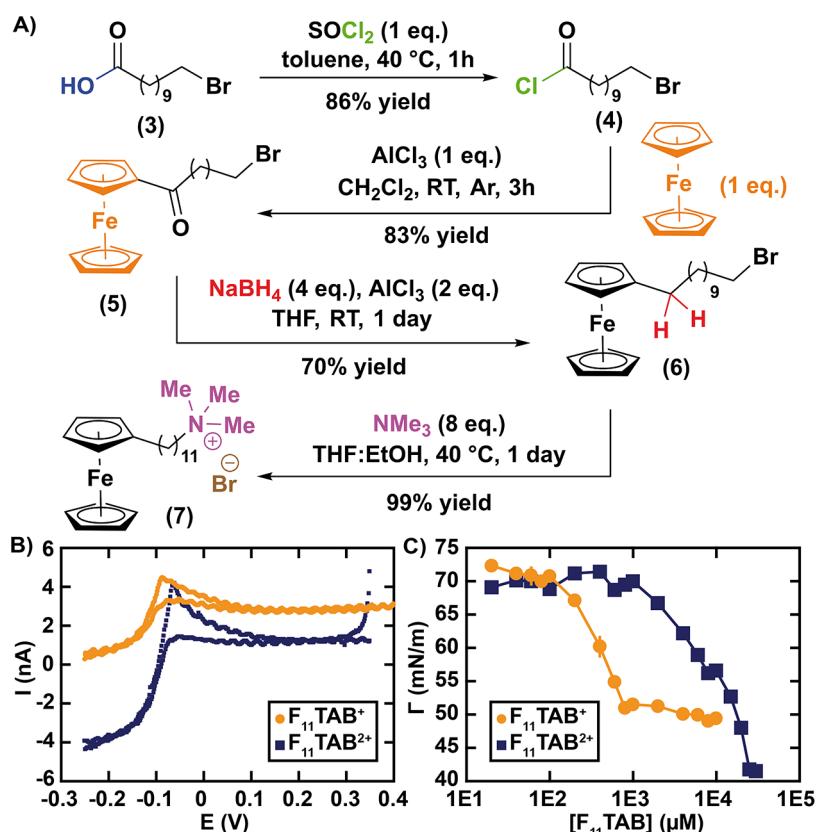
Figure 3. Synthesis and properties of $F_{11}TAB$. (A) Synthesis scheme. (B) Steady-state voltammograms (current vs potential) of the reduced ($F_{11}TAB^+$, orange disks) and oxidized ($F_{11}TAB^{2+}$, blue squares) forms of $F_{11}TAB$ (2 mM) in an aqueous solution of Li_2SO_4 (100 mM). (C) Interfacial energy in air (Γ) of water containing $F_{11}TAB^+$ or $F_{11}TAB^{2+}$, as a function of the surfactant concentration.

new principle as well as the effects of the parameters that control it are described in the following.

F_6TAB, a Short-Tail Redox-Sensitive Surfactant. Several F_nTAB surfactants have been described in literature but, in most cases, with $n \geq 8$.[31] We first synthesized a shorter-chain F_nTAB surfactant with $n = 6$, which, to our knowledge, was mentioned in only two reports[40,41] devoted to the electroactivity of F_6TAB-tethered clay, where the surfactant was obtained with a multistep synthesis and its interfacial properties were not documented. In our case, F_6TAB was obtained in a single step by Hofmann alkylation of the bromide precursor (Figure 2A, full protocol in Materials and methods). Cyclic voltammetry of F_6TAB showed a reversible redox behavior with an apparent standard potential of −0.15 V/REF (Figure 2B). The oxidized state F_6TAB^{2+} and reduced state F_6TAB^+ were quantitatively generated by bulk electrolysis at the constant potentials $E = +0.25$ and $−0.25$ V, respectively. Interestingly, the effect of F_nTAB on the interfacial energy of the water/air interface (Γ) depended on its redox state. The reduced form, with its short neutral and hydrophobic tail, had no effect on Γ for $[F_6TAB^+] < 1$ mM, with an interfacial energy close to that of pure water (70.8 ± 0.2 mN·m^{-1} under our experimental conditions), but significantly reduced Γ at higher concentrations (Figure 2C). Γ continuously decreased when $[F_6TAB^+]$ increased from 1 to 30 mM due to increasing amounts of F_6TAB^+ adsorbing at the water/air interface. Above 30 mM, solubility issues were observed and the critical micelle concentration (CMC) could thus not be reached in this system. In contrast, with the oxidized form, Γ remained constant and close to the value for water, with or without the

amount of added iron(III) used for F_6TAB oxidation (Figure S1), for the whole range of tested F_6TAB^{2+} concentrations (from 10 μM to 30 mM, Figure 2C). This is explained by the additional charge at the extremity of the tail strongly reducing the amphiphilic character of F_6TAB^{2+} and therefore its propensity to adsorb at the water/air interface and affect the interfacial energy.

$F_{11}TAB$, a Redox-Sensitive Surfactant of Higher Hydrophobicity. To explore the behavior of a redox-sensitive surfactant with a higher amphiphilic character, we synthesized $F_{11}TAB$, an analogue of F_6TAB with 5 additional carbon atoms in the alkyl chain. The synthesis was improved from the original method by Saji et al.,[42] by optimizing conditions for better yield and replacing the methylated mercury-based conversion of (5) to (6) with a safer reaction combining carbonyl activation by Lewis acid and reduction by NaBH$_4$ (Figure 3A, full protocol in Materials and methods). Cyclic voltammetry revealed a behavior similar to that of F_6TAB with identical reductive and oxidative potentials mainly controlled by the redox state of the ferrocene group (Figure 3B). The reduced form of $F_{11}TAB$ had a classical surfactant behavior affecting the water/air interfacial energy in a way similar to F_6TAB but with detectable effects starting at a much lower concentration (around 100 μM, Figure 3C) due to the longer hydrophobic tail. In that case, the CMC was reached at around 800 μM, in agreement with previous reports.[43] Interestingly and contrary to its shorter-tail homologue, $F_{11}TAB$ displayed interfacial effects even in its oxidized form, with Γ decreasing from 70 to 41 mN·m^{-1} when $[F_{11}TAB^{2+}]$ increased from 1 to 30 mM (Figure 3C). With a longer carbon chain separating the
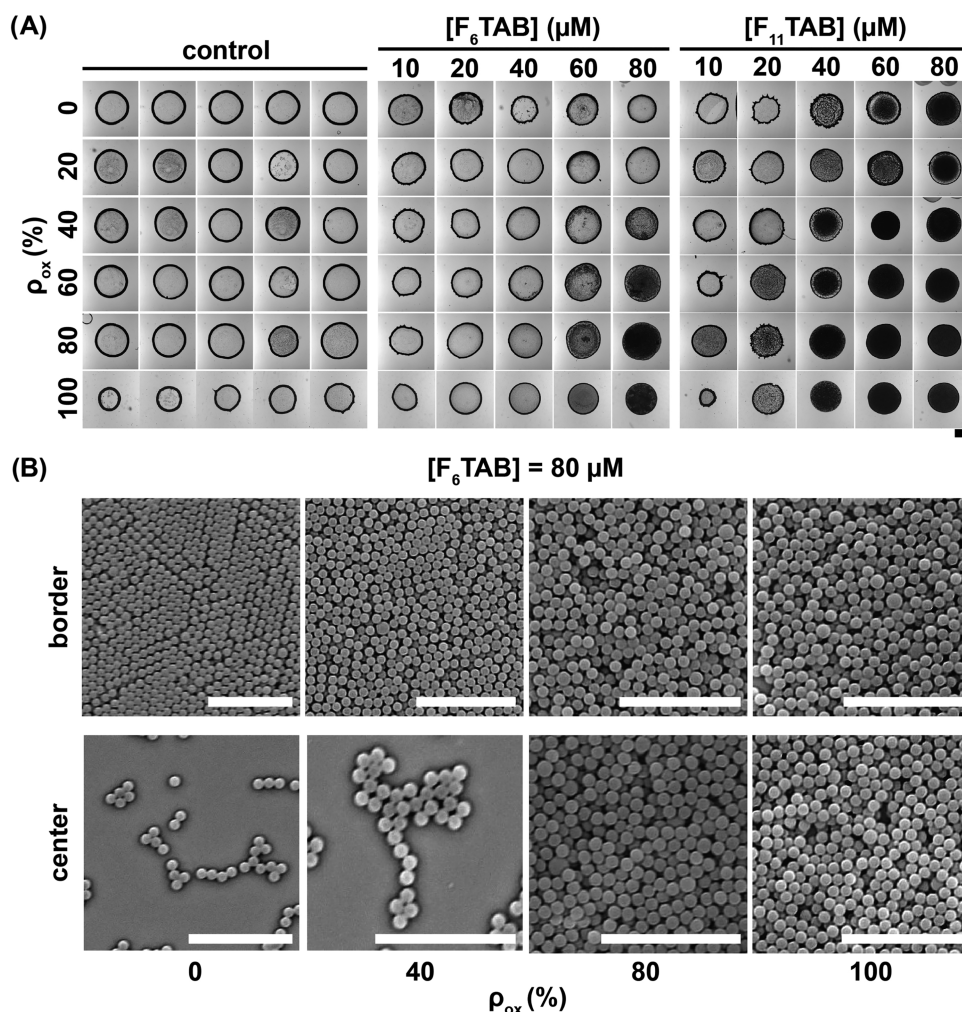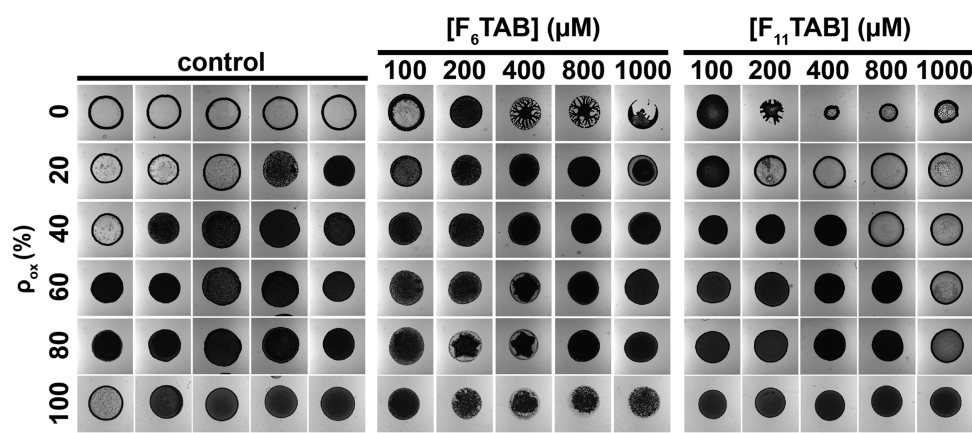
Figure 4. Redox control of the deposition patterns in the low surfactant concentration regime. (A) Representative transmission microscopy images of the deposition patterns obtained under conditions of Figure 1B, with various concentrations (columns) and oxidation rates (lines) of F_nTAB with $n = 6$ (middle panel) and $n = 11$ (right panel). The left panel (control) shows the corresponding experiments without F_nTAB but in the presence of the amount of iron(III) used to control the oxidation rate (values in Figure S4A). The scale bar is 1 mm. (B) Representative scanning electron microscopy images taken in the border (top) or in the center (bottom) of deposited patterns with $[F_6TAB] = 80\ \mu M$ at various oxidation rates. The scale bar is 10 μm.

two cationic charges at its extremities, $F_{11}TAB^{2+}$ can thus act as a bolaform surfactant capable of significantly reducing the water/air interfacial energy.

Redox Control of Deposition Patterns. Using the setup of Figure 1B, we then systematically investigated the morphology of particle patterns deposited from evaporating sessile drops containing anionic particles and F_6TAB or $F_{11}TAB$ at various concentrations and oxidation states. F_nTAB, initially synthesized in its reduced form, was oxidized by adding controlled amounts of iron(III). Absorbance spectroscopy (Figure S2) of F_nTAB^+ ($\lambda_{max} = 437$ nm) and F_nTAB^{2+} ($\lambda_{max} = 627$ nm) allowed us to extract their molar extinction coefficients (Table S2) and quantify the F_nTAB oxidation rate, defined as $\rho_{ox} = [F_nTAB^{2+}]/[F_nTAB]$, as a function of added iron(III) (Figure S3). We found that the reaction was fast and almost quantitative for both $n = 6$ (Figure S3A,C) and $n = 11$ (Figure S3B,D). This allowed us to adjust ρ_{ox} at stable values, which we named for convenience 0, 20, 40, 60, 80, and 100% (exact values given in Table S1).

We started to explore the effect of adding F_nTAB at a low concentration (<100 μM, Figure 4A). Under these conditions,

all patterns were highly reproducible with almost no depinning observed. In the absence of F_nTAB, and regardless of the amount of added iron(III) (Figure S4), particles were transported by the evaporation-driven flow toward the pinned contact line, where they accumulated to form typical ring-shaped deposition patterns (Figure 4A, left). This confirmed that the CRE robustly occurred in our system and was not affected by the small amount of ions added to control the oxidation state. In contrast, adding F_nTAB to the suspension dramatically affected the deposition pattern (Figure 4A, middle and right). With the reduced form of $F_{11}TAB$, we observed a progressive transition from a ring- to a disk-shaped pattern when $[F_{11}TAB^+]$ increased from 0 to 80 μM (Figure 4A, right). This can be explained by the progressive neutralization and hydrophobization of particles by surfactant adsorption, in agreement with zeta (ζ) potential evolution observed at lower particles and surfactant concentrations (Figure S5). This led to particles adsorbing and accumulating at the water/interface instead of being transported by the evaporation-driven flow toward the contact line. Upon evaporation, adsorbed particles were eventually deposited by the descending interface to form

Figure 5. Redox control of the deposition patterns at high surfactant concentrations (≥100 μM). Representative transmission microscopy images of the deposition patterns obtained under conditions of Figure 1B, with various concentrations (columns) and oxidation rates (lines) of F_nTAB with n = 6 (middle panel) and n = 11 (right panel). The left panel (control) shows the corresponding experiments without F_nTAB but in the presence of the amount of iron(III) used to control the oxidation rate (values in Figure S4B). The scale bar is 1 mm.

a dense disk of particles, in agreement with the known mechanism of CRE cancellation by oppositely charged surfactants.[25,26] Interestingly, this evolution was observed for all oxidation rates tested but with the appearance of the disk morphology at a characteristic F_{11}TAB concentration significantly decreasing from about 80 to 40 μM when ρ_{ox} increased from 0 to 100%, i.e., when F_{11}TAB became both more charged and more hydrophilic (Figure 4A, right). Since it is known that increasing the hydrophilicity of a surfactant decreases its efficiency to cancel the CRE[25,26] by cooperative adsorption on oppositely charged particles,[44] this result shows for the first time that the electrostatic neutralization of the particles by surfactant adsorption predominates hydrophobic effects to control the CRE. As a consequence, we could tune the morphology of the deposition pattern at a fixed F_{11}TAB concentration by simply adjusting the surfactant redox state. For instance, with [F_{11}TAB] = 20 μM, patterns evolved from a ring to a more homogeneous disk pattern when ρ_{ox} increased from 0 to 100% (Figure 4A, right). The same overall pattern evolution was observed with F_6TAB (Figure 4A, middle) but the transition from ring to disk was obtained either at a higher oxidation rate for the same surfactant concentration or at a higher surfactant concentration (80 μM) for the same oxidation evolution (Figure 1C). This shows that for a given surfactant charge, increasing the hydrophobicity of its tail increases its efficiency to cancel the CRE by favoring its capability to neutralize oppositely charged particles through cooperative adsorption,[44] an effect established for monovalent surfactants[25,26] but never observed for a higher or varying electrostatic charge of the polar head. Using scanning electron microscopy (SEM), we finally analyzed the microscopic organization of particles in the deposits obtained with 80 μM F_6TAB (Figure 4B) and with 20 μM F_{11}TAB (Figure S6). In both cases, with an increase in ρ_{ox}, we observed a progressive transition from heterogeneous deposition (ring) of ordered particles (polycrystalline assemblies) to more uniform deposition (disk) of disordered particles. Due to the progressive neutralization of particles with the increase in surfactant charge, highly repulsive particles at low ρ_{ox} were transported to the contact line by the CRE and packed there in an ordered manner[45] while at high ρ_{ox}, they became less repulsive (more "sticky") and accumulated at the water/air interface to be deposited in an amorphous manner.[26]

When F_nTAB was used at a higher concentration (100–1000 μM), a significantly different phenomenology was observed (Figure 5). Without added oxidizing salt (ρ_{ox} = 0%), even if fingering instabilities (e.g., [F_6TAB] = 400 or 800 μM) and/or contact line depinning (e.g., [F_{11}TAB] = 400–1000 μM) were observed, it appeared that increasing [F_nTAB] resulted in the maintenance of mainly disk-like deposits for n = 6 while ring-like patterns emerged for n = 11. F_{11}TAB thus behaved as a conventional cationic surfactant, with overcharging of the particles at high concentrations due to bi- to multilayered surfactant adsorption on the particle surface (Figure S5), thus preventing particles to adsorb at the water/air interface and favoring the CRE again.[25,26] In contrast, F_6TAB$^+$, which has much weaker amphiphilic properties in this concentration range (Figure 2C) than F_{11}TAB$^+$ (Figure 3C), had much less propensity to self-assemble on particle surfaces to form bi- or multilayers, resulting in the incapability to overcharge the particles (Figure S5). For ρ_{ox} > 0%, the increasing amount of multivalent salts used to control the oxidation rate resulted in the formation of disk patterns in the absence of F_nTAB (Figure 5, left). Notably, this phenomenon was correlated with the added iron(III) concentration, with rings and disks systematically occurring for added iron(III) ≤60 and ≥150 μM, respectively (Figure S7). By screening electrostatic interactions, multivalent cations at a high concentration are known to induce the adsorption of anionic particles at the water/air interface,[46] thus preventing the CRE and allowing a homogenization of the particle deposits. With its low amphiphilic properties, F_6TAB did not perturb this effect and disks were systematically obtained (Figure 5, middle). In contrast, with its stronger amphiphilic character, F_{11}TAB could counteract the salt effect and induce the formation of rings at a high concentration (Figure 5, right), probably again by multilayered adsorption of F_{11}TAB$^+$ and particle overcharging. However, increasing ρ_{ox} was accompanied by an increased relative amount of F_{11}TAB^{2+}, which had a much-reduced self-assembling character (Figure 3C). As a consequence, rings could be obtained only when a sufficient remaining amount of F_{11}TAB$^+$ was present in solution ([F_{11}TAB$^+$] > 300 μM), as shown by the correlation between ring occurrence and remaining [F_{11}TAB$^+$] (Figure S8). Hence, the total concentration of F_{11}TAB necessary to obtain a ring pattern in this regime increased with ρ_{ox} (Figure 5, right).
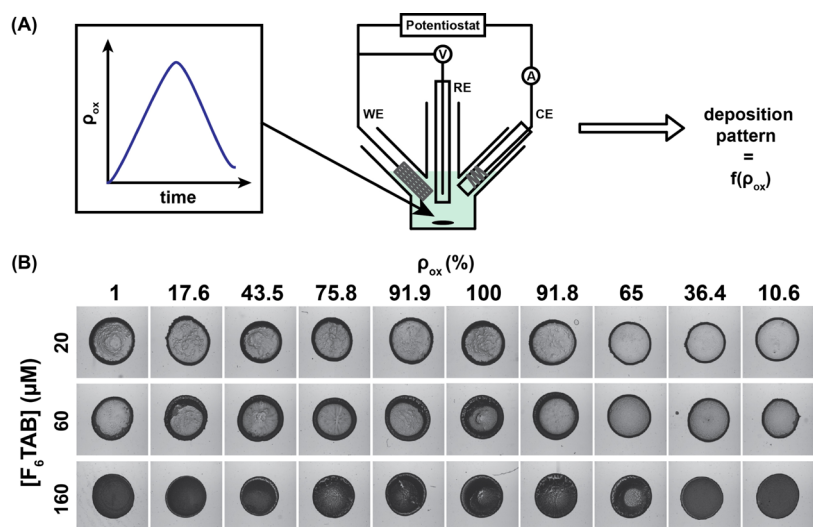
Figure 6. Electrochemical control of particle deposition in a closed system. (A) Scheme of the experiment. Without adding any chemicals, applying a constant potential in a three-electrode redox cell containing F_6TAB allows us to dynamically adjust its oxidation rate as a function of time, which in turn allows us to control the particle pattern after drop deposition and drying. (B) Representative transmission microscopy images of the deposition patterns as a function of the actual oxidation rate of F_6TAB for $[F_6$TAB$]$ = 20 μM (top), 60 μM (middle), or 160 μM (bottom).
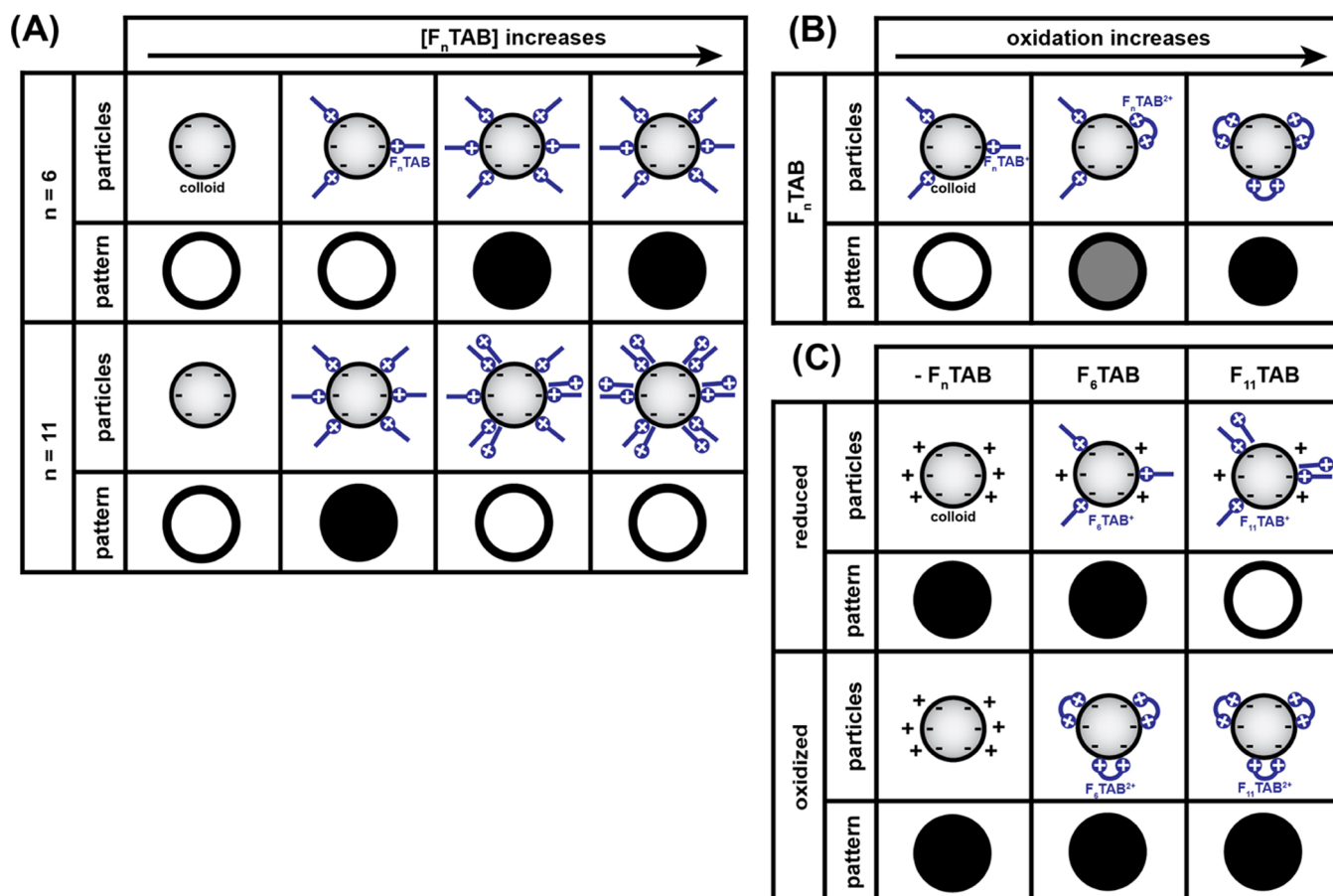
Figure 7. Schematic evolution of the colloid-surfactant interaction and resulting deposition pattern as a function of (A) F_nTAB concentration, (B) oxidation rate, and (C) in the presence of high amounts of multivalent salts.

Dynamic Electrochemical Control in a Closed System.

We demonstrated that the deposition pattern was controlled by adjusting the oxidation rate of the redox-sensitive surfactant F_nTAB obtained by the addition of oxidizing entities (iron III ions). We thus explored whether it could be possible to achieve a similar redox control but in a closed system, i.e., without adding any variable amounts of reducing or oxidizing molecules. To this end, we used a three-electrode chronoamperometry setup to adjust the oxidation rate of a F_6TAB solution (5 mM in a solution of 100 mM Li_2SO_4) in time by

applying an oxidation potential of +0.25 V followed by a reduction potential of −0.25 V (Figure 6A). This resulted in an increase of ρ_{ox} upon oxidation up to 100% followed by a decrease over time when F_6TAB was *in situ* reduced again. Aliquots of that solution were taken along the course of the reaction and the actual value of ρ_{ox} was established by absorbance. Each of these samples was diluted to a desired concentration of F_6TAB and mixed with particles (2 mg· mL^{-1}), and a drop of the resulting suspension was allowed to dry under the conditions of Figure 1B. We found that the pattern evolution upon F_6TAB electrochemical oxidation (Figure 6B) was in striking agreement with what was observed by chemically oxidizing F_6TAB (Figure 4A, middle). Regardless of ρ_{ox}, deposits displayed a ring-like morphology at a low F_6TAB concentration (20 μM) when the surfactant did not interact much with the oppositely charged particles (Figure 6B, top) and a disk-like one at a higher concentration (160 μM) when the surfactant electrostatically adsorbed and neutralized the particles (Figure 6B, bottom). Notably, at the same intermediate F_6TAB concentration (60 μM), a similar and progressive evolution from a ring-like pattern to a more homogenous disk was observed when ρ_{ox} first increased from almost 0 to 100% (Figure 6B, middle), interpreted as a signature of the increased electrostatic binding between F_6TAB and the particles upon enriching the solution in the oxidized, dicationic form of the surfactant. This consistent pattern evolution as a function of F_6TAB concentration and its oxidation rate, regardless of the nature of the oxidation method (electrochemical vs chemical), highlights the flexibility of the redox control approach and the determinant role of ρ_{ox} in directing the morphology of particle deposits. The electrochemical actuation also allowed us to reverse the stimulation by reducing F_6TAB once it was fully oxidized. We found that the resulting pattern evolution was fully reversible for all tested concentrations (Figure 6B). This was particularly noticeable for the intermediate concentration ([F_6TAB] = 60 μM) for which the patterns evolved back from a disk-like shape to a marked ring pattern when ρ_{ox} decreased from 100 to 10.6%. Note that, in the absence of F_6TAB, only ring-shaped patterns were obtained (Figure S9), showing that any significant role of remaining amounts of Li_2SO_4 after dilution can be excluded. All of these results demonstrate that the redox control of particle deposition from drying drops is not limited to chemical oxidation and can be robustly controlled through an electrochemical approach, thus allowing dynamic and additive-free modulation of the deposited patterns.

Overview. Figure 7 summarizes, in a schematic manner, the role of the main parameters we have investigated to control particle deposition in drying drops containing anionic colloids and cationic redox-sensitive surfactants. Without F_nTAB, the evaporation-driven flow accumulated charged colloids at the contact line, where repulsive particles assembled in an ordered fashion to form a polycrystalline ring. Increasing F_nTAB concentration led to a neutralization of the particles and their accumulation at the water/air interface to form a uniform and amorphous disk-shaped deposit after drying (Figure 7A). This is similar to what can be obtained with conventional salts at millimolar concentrations except that this effect occurred here in a micromolar concentration regime due to the cooperative adsorption of surfactants on the oppositely charged surface of the anionic colloids. This self-assembly is all the more efficient that surfactants are hydrophobic, explaining that, for a given oxidation rate, $F_{11}TAB$ led to the formation of a disk at a lower

concentration than F_6TAB (Figure 7A). A further increase in $F_{11}TAB$ concentration led to the formation of rings again due to the overcharging of the particles by multilayered adsorption of the surfactant on their surface, in agreement with the known effect of cationic surfactants on the CRE.[25,26] However, we observed for the first time that this was not the case for a short-hydrophobic tail surfactant such as F_6TAB because its reduced self-assembly ability prevented from efficient particle overcharging. Increasing hydrophobic effects, by favoring surfactant self-assembly and cooperative adsorption on oppositely charged nanoparticles, thus promoted both the formation of uniform disk patterns at low surfactant concentrations and the reappearance of rings at higher concentrations. Interestingly, we found that oxidizing F_nTAB^+, although decreasing its hydrophobic and self-assembly character, led to a transition from a ring to disk pattern for both F_6TAB and $F_{11}TAB$ (Figure 7B). This was again due to the neutralization of particles, which, at a fixed F_nTAB concentration, was more efficient at a higher fraction of the dicationic form of the surfactant, i.e., at a higher oxidation rate. This emphasizes the predominant role of electrostatics in controlling the CRE in oppositely charged particle-surfactant systems and how surfactant self-assembly can modulate it. Increasing the surfactant chain length thus decreased the concentration at which the ring-to-disk transition was obtained either by adding the surfactant of a given oxidation rate or by oxidizing a fixed concentration of the surfactant (Figure 4A). Finally, studying high concentrations of the surfactant (Figure 5) involved high amounts of iron(III)/iron(II) and thus allowed to have insights on the effect of surfactants versus that of multivalent salts present in the solution (Figure 7C). At high salt concentrations, disk patterns were systematically obtained in the absence of surfactants. When surfactants were added, this was unchanged as long as surfactants were not hydrophobic enough to create multilayers and overcharge the particles. This was the case for F_6TAB^+ and F_6TAB^{2+} (too short tail) and $F_{11}TAB^{2+}$ (too polar). Only sufficiently large amounts of $F_{11}TAB^+$ (high $F_{11}TAB$ concentration and low oxidation rate) could overcharge the particles and avoid their accumulation at the water/air interface, leading to ring-shaped patterns.

■ CONCLUSIONS

We showed for the first time how the deposition pattern from a drying sessile drop could be controlled by a redox stimulus at both macroscopic (from ring to disk morphology) and microscopic (from crystalline to amorphous) levels. Achieved by simply adding a redox-sensitive surfactant in a colloidal suspension drop, the method allowed not only a full cancellation of the coffee-ring effect (CRE) but also a reproducible and user-defined adjustment of the deposit morphology, ranging from a marked ring to a homogenous disk pattern when typically switching from reductive to oxidizing conditions. We demonstrated that the oxidation rate of the surfactant can be tuned either chemically by simply adding oxidizing molecules or electrochemically through the in situ application of a potential in an additive-free manner, highlighting the robustness, flexibility, and reversible character of the approach. At a fundamental level, this study significantly improved our understanding of the general role of surfactants in controlling the CRE of oppositely charged colloids, with the following points that are worth being highlighted: (1) by promoting particle accumulation at the water/air interface,

electrostatic screening and particle neutralization are key factors in the cancellation of the CRE; (2) increasing surfactant charge amplifies the phenomenon and overcomes hydrophobic effects; (3) the presence of the hydrophobic tail, by promoting self-assembly, makes surfactants behave (i) as "supersalts" to neutralize particles and favor CRE cancellation at a very low concentration and (ii) as "antisalts" at high concentrations by overcharging particles and inducing CRE again; and (4) as a consequence, increasing surfactant hydrophobicity shifts the cancellation of the CRE to a lower surfactant concentration while also favoring its reappearance by particle overcharging. Overall, this work brings new practical and fundamental solutions to cancel the CRE in many situations when it is deleterious or, on the contrary, to harness it to organize particles on surfaces in a controlled manner. By straightforward adjustment of the redox state, fine tuning of the particle deposition can be done from the overall distribution of particles on a surface to their microscopic organization. Conversely, this principle makes it now possible to get information on the redox state of a sample liquid by simply visualizing the deposition pattern left by a drying μL-sized drop, thus constituting a novel and advantageously simple concept for rapid and portable diagnostics with applications ranging from material analysis to point-of-care biomedical monitoring.

■ ASSOCIATED CONTENT

ⓈI Supporting Information

The Supporting Information is available free of charge at https://pubs.acs.org/doi/10.1021/acsami.1c18933.

> Interfacial energy as a function of iron(III) (Figure S1); absorbance spectra of F_6TAB and F_{11}TAB in both reduced and oxidized states (Figure S2); characterizations of the chemical oxidation of F_6TAB and F_{11}TAB by iron(III) including kinetics (Figure S3); matrix of iron(III) concentrations used to control the oxidation rates (Figure S4); ζ-potential of particles as a function of F_nTAB concentration (Figure S5); SEM images of the patterns obtained with F_{11}TAB (Figure S6); phase diagram of the deposit morphology as a function of added iron(III) (Figure S7); phase diagram of the deposit morphology as a function of F_{11}TAB$^+$ concentration (Figure S8); deposition patterns in the conditions of Figure 6B in the absence of F_6TAB (Figure S9); named and actual values of the oxidation rates (Table S1); molar extinction coefficients for F_6TAB and F_{11}TAB in both reduced and oxidized states (Table S2) (PDF)

■ AUTHOR INFORMATION

Corresponding Author

Damien Baigl − *PASTEUR, Department of Chemistry, École Normale Supérieure, PSL University, Sorbonne Université, CNRS, 75005 Paris, France;* ⓞ orcid.org/0000-0003-1772-3080; Email: damien.baigl@ens.psl.eu

Authors

Pauline E. Galy − *PASTEUR, Department of Chemistry, École Normale Supérieure, PSL University, Sorbonne Université, CNRS, 75005 Paris, France*

Tiffany Guitton-Spassky − *PASTEUR, Department of Chemistry, École Normale Supérieure, PSL University, Sorbonne Université, CNRS, 75005 Paris, France*

Catherine Sella − *PASTEUR, Department of Chemistry, École Normale Supérieure, PSL University, Sorbonne Université, CNRS, 75005 Paris, France*

Laurent Thouin − *PASTEUR, Department of Chemistry, École Normale Supérieure, PSL University, Sorbonne Université, CNRS, 75005 Paris, France;* ⓞ orcid.org/0000-0002-2635-5825

Maxime R. Vitale − *UMR 7203, Department of Chemistry, Ecole Normale Supérieure, PSL University, Sorbonne Université, CNRS, 75005 Paris, France;* ⓞ orcid.org/0000-0002-6740-2472

Complete contact information is available at:
https://pubs.acs.org/10.1021/acsami.1c18933

Author Contributions

The manuscript was written through contributions of all authors. All authors have given approval to the final version of the manuscript.

Notes

The authors declare no competing financial interest.

■ ACKNOWLEDGMENTS

■ REFERENCES

(1) Deegan, R. D.; Bakajin, O.; Dupont, T. F.; Huber, G.; Nagel, S. R.; Witten, T. A. Capillary Flow as the Cause of Ring Stains from Dried Liquid Drops. *Nature* **1997**, *389*, 827−829.

(2) Poulichet, V.; Morel, M.; Rudiuk, S.; Baigl, D. Liquid-Liquid Coffee-Ring Effect. *J. Colloid Interface Sci.* **2020**, *573*, 370−375.

(3) Larson, R. G. Re-Shaping the Coffee Ring. *Angew. Chem., Int. Ed.* **2012**, *51*, 2546−2548.

(4) Larson, R. G. Transport and Deposition Patterns in Drying Sessile Droplets. *AIChE J.* **2014**, *60*, 1538−1571.

(5) Park, J.; Moon, J. Control of Colloidal Particle Deposit Patterns within Picoliter Droplets Ejected by Ink-Jet Printing. *Langmuir* **2006**, *22*, 3506−3513.

(6) Blossey, R.; Bosio, A. Contact Line Deposits on CDNA Microarrays: A "Twin-Spot Effect". *Langmuir* **2002**, *18*, 2952−2954.

(7) Dugas, V.; Broutin, J.; Souteyrand, E. Droplet Evaporation Study Applied to DNA Chip Manufacturing. *Langmuir* **2005**, *21*, 9130−9136.

(8) Deng, Y.; Zhu, X.-Y.; Kienlen, T.; Guo, A. Transport at the Air/Water Interface Is the Reason for Rings in Protein Microarrays. *J. Am. Chem. Soc.* **2006**, *128*, 2768−2769.

(9) Anyfantakis, M.; Baigl, D. Manipulating the Coffee-Ring Effect: Interactions at Work. *ChemPhysChem* **2015**, *16*, 2726−2734.

(10) Zhang, Z.; Zhang, X.; Xin, Z.; Deng, M.; Wen, Y.; Song, Y. Controlled Inkjetting of a Conductive Pattern of Silver Nanoparticles Based on the Coffee-Ring Effect. *Adv. Mater.* **2013**, *25*, 6714−6718.

(11) Kuang, M.; Wang, L.; Song, Y. Controllable Printing Droplets for High-Resolution Patterns. *Adv. Mater.* **2014**, *26*, 6950−6958.

(12) Varanakkottu, S. N.; Anyfantakis, M.; Morel, M.; Rudiuk, S.; Baigl, D. Light-Directed Particle Patterning by Evaporative Optical Marangoni Assembly. *Nano Lett.* **2016**, *16*, 644−650.

(13) Anyfantakis, M.; Varanakkottu, S. N.; Rudiuk, S.; Morel, M.; Baigl, D. Evaporative Optical Marangoni Assembly: Tailoring the Three-Dimensional Morphology of Individual Deposits of Nanoparticles from Sessile Drops. *ACS Appl. Mater. Interfaces* **2017**, *9*, 37435−37445.

(14) Trantum, J. R.; Wright, D. W.; Haselton, F. R. Biomarker-Mediated Disruption of Coffee-Ring Formation as a Low Resource Diagnostic Indicator. *Langmuir* **2012**, *28*, 2187−2193.

(15) Wen, J. T.; Ho, C. M.; Lillehoj, P. B. Coffee Ring Aptasensor for Rapid Protein Detection. *Langmuir* **2013**, *29*, 8440−8446.

(16) Gulka, C. P.; Swartz, J. D.; Trantum, J. R.; Davis, K. M.; Peak, C. M.; Denton, A. J.; Haselton, F. R.; Wright, D. W. Coffee Rings as Low-Resource Diagnostics: Detection of the Malaria Biomarker Plasmodium Falciparum Histidine-Rich Protein-II Using a Surface-Coupled Ring of Ni(II)NTA Gold-Plated Polystyrene Particles. *ACS Appl. Mater. Interfaces* **2014**, *6*, 6257−6263.

(17) Li, Y.; Zhao, Z.; Lam, M. L.; Liu, W.; Yeung, P. P.; Chieng, C.-C.; Chen, T.-H. Hybridization-Induced Suppression of Coffee Ring Effect for Nucleic Acid Detection. *Sens. Actuators, B* **2015**, *206*, 56−64.

(18) Devineau, S.; Anyfantakis, M.; Marichal, L.; Kiger, L.; Morel, M.; Rudiuk, S.; Baigl, D. Protein Adsorption and Reorganization on Nanoparticles Probed by the Coffee-Ring Effect: Application to Single Point Mutation Detection. *J. Am. Chem. Soc.* **2016**, *138*, 11623−11632.

(19) Mampallil, D.; Eral, H. B.; van den Ende, D.; Mugele, F. Control of Evaporating Complex Fluids through Electrowetting. *Soft Matter* **2012**, *8*, 10614−10617.

(20) Wray, A. W.; Papageorgiou, D. T.; Craster, R. V.; Sefiane, K.; Matar, O. K. Electrostatic Suppression of the "Coffee Stain Effect.". *Langmuir* **2014**, *30*, 5849−5858.

(21) Malinowski, R.; Volpe, G.; Parkin, I. P.; Volpe, G. Dynamic Control of Particle Deposition in Evaporating Droplets by an External Point Source of Vapor. *J. Phys. Chem. Lett.* **2018**, *9*, 659−664.

(22) Sáenz, P. J.; Wray, A. W.; Che, Z.; Matar, O. K.; Valluri, P.; Kim, J.; Sefiane, K. Dynamics and Universal Scaling Law in Geometrically-Controlled Sessile Drop Evaporation. *Nat. Commun.* **2017**, *8*, No. 14783.

(23) Talbot, E. L.; Yang, L.; Berson, A.; Bain, C. D. Control of the Particle Distribution in Inkjet Printing through an Evaporation-Driven Sol−Gel Transition. *ACS Appl. Mater. Interfaces* **2014**, *6*, 9572−9583.

(24) Still, T.; Yunker, P. J.; Yodh, A. G. Surfactant-Induced Marangoni Eddies Alter the Coffee-Rings of Evaporating Colloidal Drops. *Langmuir* **2012**, *28*, 4984−4988.

(25) Anyfantakis, M.; Baigl, D. Dynamic Photocontrol of the Coffee-Ring Effect with Optically Tunable Particle Stickiness. *Angew. Chem., Int. Ed.* **2014**, *53*, 14077−14081.

(26) Anyfantakis, M.; Geng, Z.; Morel, M.; Rudiuk, S.; Baigl, D. Modulation of the Coffee-Ring Effect in Particle/Surfactant Mixtures: The Importance of Particle−Interface Interactions. *Langmuir* **2015**, *31*, 4113−4120.

(27) Diguet, A.; Guillermic, R. M.; Magome, N.; Saint-Jalmes, A.; Chen, Y.; Yoshikawa, K.; Baigl, D. Photomanipulation of a Droplet by the Chromocapillary Effect. *Angew. Chem., Int. Ed.* **2009**, *48*, 9281−9284.

(28) Vialetto, J.; Anyfantakis, M.; Rudiuk, S.; Morel, M.; Baigl, D. Photoswitchable Dissipative Two-Dimensional Colloidal Crystals. *Angew. Chem., Int. Ed.* **2019**, *58*, 9145−9149.

(29) Saji, T.; Hoshino, K.; Aoyagui, S. Reversible Formation and Disruption of Micelles by Control of the Redox State of the Surfactant Tail Group. *J. Chem. Soc. Chem. Commun.* **1985**, *13*, 865−866.

(30) Hoshino, K.; Saji, T. Electrochemical Formation of an Organic Thin Film by Disruption of Micelles. *J. Am. Chem. Soc.* **1987**, *109*, 5881−5883.

(31) Saji, T.; Hoshino, K.; Ishii, Y.; Goto, M. Formation of Organic Thin Films by Electrolysis of Surfactants with the Ferrocenyl Moiety. *J. Am. Chem. Soc.* **1991**, *113*, 450−456.

(32) Muñoz, S.; Gokel, G. W. Redox-Switched Vesicle Formation from Two Novel, Structurally Distinct Metalloamphiphiles. *J. Am. Chem. Soc.* **1993**, *115*, 4899−4900.

(33) Takahashi, Y.; Koizumi, N.; Kondo, Y. Demulsification of Redox-Active Emulsions by Chemical Oxidation. *Langmuir* **2016**, *32*, 7556−7563.

(34) Hays, M. E.; Jewell, C. M.; Lynn, D. M.; Abbott, N. L. Reversible Condensation of DNA Using a Redox-Active Surfactant. *Langmuir* **2007**, *23*, 5609−5614.

(35) Gallardo, B. S.; Hwa, M. J.; Abbott, N. L. In Situ and Reversible Control of the Surface Activity of Ferrocenyl Surfactants in Aqueous Solutions. *Langmuir* **1995**, *11*, 4209−4212.

(36) Bennett, D. E.; Gallardo, B. S.; Abbott, N. L. Dispensing Surfactants from Electrodes: Marangoni Phenomenon at the Surface of Aqueous Solutions of (11-Ferrocenylundecyl)Trimethylammonium Bromide. *J. Am. Chem. Soc.* **1996**, *118*, 6499−6505.

(37) Bai, G.; Graham, M. D.; Abbott, N. L. Role of Desorption Kinetics in Determining Marangoni Flows Generated by Using Electrochemical Methods and Redox-Active Surfactants. *Langmuir* **2005**, *21*, 2235−2241.

(38) García-Barrantes, P. M.; Lamoureux, G. V.; Pérez, A. L.; García-Sánchez, R. N.; Martínez, A. R.; San Feliciano, A. Synthesis and Biological Evaluation of Novel Ferrocene-Naphthoquinones as Antiplasmodial Agents. *Eur. J. Med. Chem.* **2013**, *70*, 548−557.

(39) Li, C.; Ren, B.; Zhang, Y.; Cheng, Z.; Liu, X.; Tong, Z. A Novel Ferroceneylazobenzene Self-Assembled Monolayer on an ITO Electrode: Photochemical and Electrochemical Behaviors. *Langmuir* **2008**, *24*, 12911−12918.

(40) Swearingen, C.; Macha, S.; Fitch, A. Ferrocene Groups Tethered to Clay Surfaces. *J. Electrochem. Soc.* **2002**, *149*, No. E103.

(41) Swearingen, C.; Wu, J.; Stucki, J.; Fitch, A. Use of Ferrocenyl Surfactants of Varying Chain Lengths to Study Electron Transfer Reactions in Native Montmorillonite Clay. *Environ. Sci. Technol.* **2004**, *38*, 5598−5603.

(42) Saji, T.; Hoshino, K.; Aoyagui, S. Reversible Formation and Disruption of Micelles by Control of the Redox State of the Surfactant Tail Group. *J. Chem. Soc. Chem. Commun.* **1985**, *53*, No. 865.

(43) Gallardo, B. S.; Metcalfe, K. L.; Abbott, N. L. Ferrocenyl Surfactants at the Surface of Water: Principles for Active Control of Interfacial Properties. *Langmuir* **1996**, *12*, 4116−4124.

(44) Deleurence, R.; Parneix, C.; Monteux, C. Mixtures of Latex Particles and the Surfactant of Opposite Charge Used as Interface Stabilizers—Influence of Particle Contact Angle, Zeta Potential, Flocculation and Shear Energy. *Soft Matter* **2014**, *10*, 7088−7095.

(45) Marín, Á. G.; Gelderblom, H.; Lohse, D.; Snoeijer, J. H. Order-to-Disorder Transition in Ring-Shaped Colloidal Stains. *Phys. Rev. Lett.* **2011**, *107*, No. 085502.

(46) Abdel-Fattah, A. I.; El-Genk, M. S. Sorption of Hydrophobic, Negatively Charged Microspheres onto a Stagnant Air/Water Interface. *J. Colloid Interface Sci.* **1998**, *202*, 417−429.